Title

Hierarchical supramolecular assembly of a single peptoid polymer into a planar nanobrush with two distinct molecular packing motifs

Journal

Proceedings of the National Academy of Sciences of the United States of America, 117(50)

ISSN

0027-8424

Authors

Sun, Jing

Wang, Zhiwei

Zhu, Chenhui

et al.

Publication Date

2020-12-15

DOI

10.1073/pnas.2011816117

Peer reviewed

Hierarchical supramolecular assembly of a single peptoid polymer into a planar nanobrush with two distinct molecular packing motifs

Jing Sun[a,1], Zhiwei Wang[a], Chenhui Zhu[b], Meiyao Wang[a], Zhekun Shi[a], Yuhan Wei[a], Xiaohui Fu[a], Xuesi Chen[c,1], and Ronald N. Zuckermann[d,1]

[a]Key Laboratory of Biobased Polymer Materials, College of Polymer Science and Engineering, Qingdao University of Science and Technology, 266042 Qingdao, China; [b]Advanced Light Source, Lawrence Berkeley National Laboratory, Berkeley, CA 94720; [c]Key Laboratory of Polymer Ecomaterials, Changchun Institute of Applied Chemistry, Chinese Academy of Sciences, 130022 Changchun, China; and [d]Molecular Foundry, Lawrence Berkeley National Laboratory, Berkeley, CA 94720

Edited by Kristi S. Anseth, University of Colorado Boulder, Boulder, CO, and approved November 3, 2020 (received for review June 8, 2020)

Hierarchical nanomaterials have received increasing interest for many applications. Here, we report a facile programmable strategy based on an embedded segmental crystallinity design to prepare unprecedented supramolecular planar nanobrush-like structures composed of two distinct molecular packing motifs, by the self-assembly of one particular diblock copolymer poly(ethylene glycol)-*block*-poly(*N*-octylglycine) in a one-pot preparation. We demonstrate that the superstructures result from the temperature-controlled hierarchical self-assembly of preformed spherical micelles by optimizing the crystallization–solvophobicity balance. Particularly remarkable is that these micelles first assemble into linear arrays at elevated temperatures, which, upon cooling, subsequently template further lateral, crystallization-driven assembly in a living manner. Addition of the diblock copolymer chains to the growing nanostructure occurs via a loosely organized micellar intermediate state, which undergoes an unfolding transition to the final crystalline state in the nanobrush. This assembly mechanism is distinct from previous crystallization-driven approaches which occur via unimer addition, and is more akin to protein crystallization. Interestingly, nanobrush formation is conserved over a variety of preparation pathways. The precise control ability over the superstructure, combined with the excellent biocompatibility of polypeptoids, offers great potential for nanomaterials inaccessible previously for a broad range of advanced applications.

self-assembly | polypeptoid | diblock copolymer | crystallization | solvophobicity

Biomacromolecules fold and assemble into complex, well-organized hierarchical structures by a network of noncovalent interactions, which enable tremendous architectural diversity in nature (1, 2). For example, polypeptide chains encoded with assembly information in their monomer sequence can fold into highly ordered conformations, which give rise to their biological functionality (3). Inspired by these intricate natural designs, numerous efforts have been devoted to fabricating hierarchical nanostructures using synthetic polymeric materials (4–11). However, the precision control over the assembly process and structure across many length scales, as commonly seen in biomacromolecules, remains a challenging task (12). This is because the assembly information content encoded within synthetic macromolecules is considerably lower.

Synthetic chemists have looked to develop polymer systems that retain many of the structural features found in natural biopolymers. Bioinspired synthetic polymers have attracted growing attention, because of their inherent structural advantages, facile synthetic approaches, and improved stability, to serve as promising materials for the de novo design and assembly of hierarchical nanostructures. In particular, polypeptoids are a class of peptidomimetic polymers based on a polar amide backbone (13–15). This differs substantially from carbon-chain polymers such as polyethylene and polypropylene. The amide groups impart higher water solubility, excellent biocompatibility, the opportunity for multiple backbone–backbone interactions, and enable a wide range of bioactivities. Polypeptoids are devoid of hydrogen bond donating sites and chirality on the backbone due to the *N* substitution. This simplifies the complex molecular interactions inherent in peptidomimetic materials, resulting in efficient engineering and controllable architecture construction. For example, polypeptoids with alkyl side chain groups are semicrystalline with inherent characteristic packing domains, which is in sharp contrast to polypeptides (16–19).

Macromolecular crystallization is an essential process in both nature and materials manufacturing. The self-assembly of block copolymers containing crystalline blocks generally enables the formation of multiscale architectures with a high level of control over morphology and dimension (20, 21). Recently, living crystallization-driven self-assembly has been demonstrated to be an effective strategy to precisely control the nanoscale morphology (22–30). Inspired by the natural encoded information-guided self-assembly, we based our design on a hydrophobic poly(*N*-alkylglycine) peptoid block that is known to form a rectangular crystalline lattice with controllable dimension and

Significance

The preparation of hierarchical biomimetic nanostructures remains a challenging task. Bioinspired peptoid polymers offer a promising opportunity to encode assembly information within the component chains. Here, we report a one-pot preparation of planar nanobrush structures from poly(ethyleneglycol)-*block*-poly(*N*-octylglycine) based on tuning the interplay of crystallization and solvophobicity. Each nanobrush assembly is composed of two distinct structural domains, which form sequentially by control of the solution temperature, and contain distinct molecular packing motifs. Micellar intermediates first assemble into linear arrays at elevated temperature in a mesophase state, followed by lateral, crystallization-driven growth in a living manner upon cooling. Precise control over the nanobrush dimensions could be achieved. The structural tunability and excellent biocompatibility of polypeptoids offer great potential for nanomaterials inaccessible previously.

Author contributions: J.S. designed research; J.S., Z.W., C.Z., M.W., Z.S., Y.W., and X.F. performed research; C.Z. and X.C. contributed new reagents/analytic tools; J.S., Z.W., X.C., and R.N.Z. analyzed data; and J.S., X.C., and R.N.Z. wrote the paper.

The authors declare no competing interest.

This article is a PNAS Direct Submission.

[1]To whom correspondence may be addressed. Email: jingsun@qust.edu.cn, xschen@ciac.ac.cn, or rnzuckermann@lbl.gov.

This article contains supporting information online at https://www.pnas.org/lookup/suppl/doi:10.1073/pnas.2011816117/-/DCSupplemental.

First published December 1, 2020.

two melting transitions (31). It is also known that solvophobic interaction is the predominant driving force for assembly of systems with solvophobic segments (5). The delicate interplay between crystallization and solvophobicity is essential for biomolecule self-assembly (32), which potentially serves as a powerful strategy for self-assembly of block copolymers. Thus, we embarked on a study of block copolymers, where the relative strength of these two factors could be systematically adjusted. By optimizing the balance between these two factors, we discovered that poly(ethylene glycol)-*block*-poly(*N*-octylglycine) (PEG-*b*-PNOG) formed unique supramolecular planar nanobrush architectures in high yield. We developed a simple temperature-controlled assembly strategy to create superbrushes consisting of two distinct packing domains: a long core fiber, or "spine," with lengths up to ~2.0 μm, and laterally splayed shorter fibers of ~400 nm in length on apposed side surfaces of the spine. We further demonstrated that this lateral growth of the brush exhibits living growth manner via a micelle intermediate, fairly distinct from known living crystallization-driven self-assembly approaches (16, 23, 33), where assemblies grow via the direct attachment of block unimers. Our results coincide with the reported "particle attachment" strategy observed in a range of biomacromolecules and small molecules, where intermediate higher-ordered species form in solution prior to their attachment to the crystal lattice, in contrast to monomer-by-monomer crystal growth (1, 32, 34, 35). Such pathways allow for the optimization of interactions to facilitate thermodynamic favored transition from the initial species to hierarchical assemblies.

Results and Discussion

Self-Assembly of Brush-Like Superstructures. A series of diblock copolypeptoids containing a hydrophobic *N*-alkylglycine peptoid block and a polar PEG block were synthesized by ring-opening polymerization (ROP) of *N*-substituted *N*-carboxyanhydride (NNCA) monomers and characterized carefully (*SI Appendix*, Figs. S1–S6 and Tables S1 and S2) (36). The self-assembly of the block copolymers was performed in methanol, which can dissolve PEG but is a nonsolvent for the polypeptoid block. In a general preparation procedure, PEG-*b*-PNOG was dispersed in methanol at a concentration of 0.5 mg/mL that results in a suspension, heated to 65 °C and held for 2 h, followed by slow cooling to room temperature and incubating for 1 d. Brush-like superstructures that resemble a planar "shish-kebab" were produced exclusively and in high yield from PEG_{112}-*b*-$PNOG_{54}$, as observed by negative stained transmission electron microscopy (TEM) (Fig. 1*A*). The subscripts denote the average degree of polymerization (DP) of each block. The superbrushes comprise two distinct components: a long core fiber, or spine, in length, and laterally splayed fiber arrays on opposed surfaces of the central spine in width. The length of the brush can reach up to ~2.0 μm, and the lateral width is typically in the range of 380 nm to 410 nm. Atomic force microscope (AFM) imaging of dried nanobrushes shows the height of the central spine to be in the range of 10 nm to 12 nm, which is distinctly higher than the lateral fibers (6 nm to 7 nm) (Fig. 1*B*). This suggests that each region has a different packing geometry of the polymer chains. It is remarkable that the heights of the spines and lateral fibers are quite consistent across many nanobrush assemblies. Cryogenic electron microscopy (cryo-EM) was further used to study the nanostructures in the solution state by preparing an unstained vitreous PEG_{112}-*b*-$PNOG_{54}$ thin film. The brush-like superstructures are observed in solution in a high yield (Fig. 1*C*).

Spine Formation at Elevated Temperature. The detailed structural evolution was further examined to shed light on the growth kinetics. The block copolymers are insoluble at room temperature in methanol, irrespective of the stirring time, while, at elevated temperature, the chain mobility of PNOG increases largely. Note that the bulk samples exhibit two distinct melting transitions by differential scanning calorimetry (DSC) endotherms in most cases, arising from the partial loss of order with temperature (T_{m1} and T_{m2} are denoted as the low and high melting temperature, respectively, in *SI Appendix*, Fig. S6) (31). As the temperature rises above T_{m1} in the vicinity of ~48 °C, the PNOG block transitions into a mesophase, where the loss of order in a

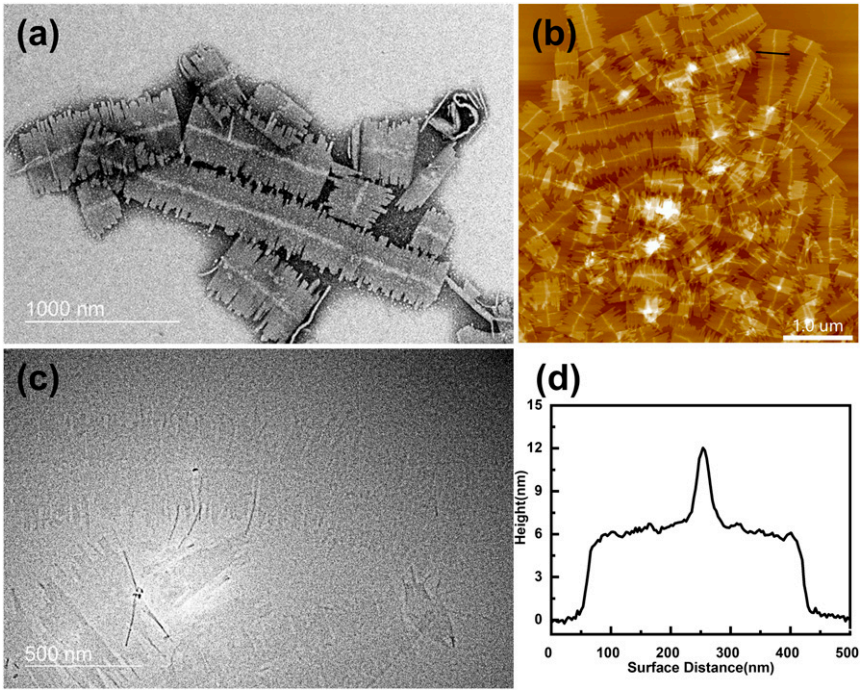

Fig. 1. Microscopy analysis of brush-like superstructure. (*A*) TEM, (*B*) AFM, and (*C*) Cryo-EM images of PEG_{112}-*b*-$PNOG_{54}$ cooled to room temperature and incubated for 24 h after annealing at 65 °C in methanol at a concentration of 0.5 mg/mL, and (*D*) the corresponding height profile of one nanobrush in *B* as indicated by the black line.

specific direction facilitates the chain mobility. In many systems, reasonable chain mobility of a block is a prerequisite for the self-assembly of block copolymer (37). With the assistance of the soluble PEG block, the copolymer self-assembles to yield a slightly cloudy solution. AFM images of the sample solution in methanol after being held at 65 °C for 5 min show a large amount of spherical micelles, and a few fibers with a mean contour length (L_n) of 166 nm (polydispersity index [PDI] = L_w/L_n = 1.09) (Fig. 2*A*). The fibers are observed to be assembled by fusion of micelles in the appearance of a necklace-like morphology, as shown in Fig. 2*B*. The spheres and fibers have quite close heights (~6.5 nm) and diameters (~21.4 nm), suggesting a similar packing geometry of the polymer chains. In addition, the diameter of the micelles is around 3 times their height, confirming their spherical shape rather than flat nanodisks. In both cases, the PEG segments are expected to form soluble corona layers, which wrap around the insoluble PNOG cores. After a 10-min incubation, the L_n increases to 242 nm with a comparable PDI of 1.10. As the solution is further incubated for 20 min and 30 min at 65 °C, the L_n of the spine increases to 564 nm and 1.04 μm, respectively. Note that the height of the spine also increases to ~11 nm, while the diameter increases to ~28 nm accordingly during this period. This is possibly because the aggregation number increases to reduce the interfacial energy attributed to PEG corona chains, consistent with the crew-cut micelle theory (38). Meanwhile, the PNOG core is also likely to organize into a more ordered structure. Further incubation at 65 °C results in a consistent L_n value and PDI (*SI Appendix*, Table S3). We thus employed a 2-h annealing time as a general procedure to reach an equilibrium state for subsequent experiments. Note that a few spheres are still present with the fibers in solution after 24 h (Fig. 2*H*), possibly due to an interplay of concentration-dependent enthalpic and entropic considerations (39). In contrast to the interfacial energy effects which facilitate the cohesion of spheres, the deformation of the PEG blocks results in a free energy penalty that inhibits the aggregation of the spheres. The interplay of these two effects dominates the equilibrium structure of the system. We therefore presume that most of the spheres are consumed into fibers, while the remainder become too dilute to fuse. The coexistence of assemblies with different morphologies has been reported in many systems (40). To confirm this, we investigated the concentration effect on the L_n of the fibers. As the concentration increases from 0.5 mg/mL to 3 mg/mL at 65 °C, the L_n value increases substantially from 1.04 μm to 4.20 μm (*SI Appendix*, Fig. S7).

To further study the formation mechanism, we prepared a series of block copolymers with different DP of PNOG and systematically studied the effects of the concentration, DP of PNOG, and temperature on the L_n. In most cases, increasing the polypeptoid concentration results in a significant increase in L_n (*SI Appendix*, Fig. S8*A*), particularly for the polymers with low DP of PNOG. We also plotted L_n as a function of DP of PNOG. As the DP of PNOG increases, the L_n of the fiber decreases (*SI Appendix*, Fig. S8*B*). The increased DP of PNOG results in reduced compatibility in methanol, which disfavors the formation of long fibers. Note that the diameters of the spheres assembled from all of the samples are very similar despite differences in the DP of PNOG (*SI Appendix*, Fig. S9), possibly due to different

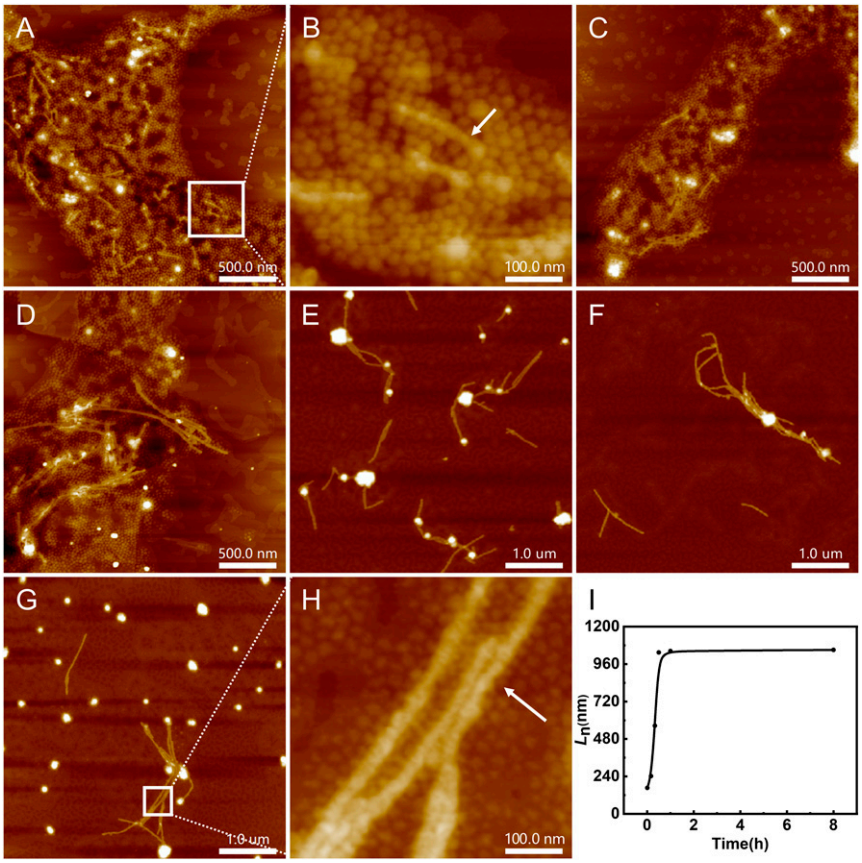

Fig. 2. Structural evolution of spine as a function of time. AFM images of PEG_{112}-*b*-$PNOG_{54}$ annealed at 65 °C for (*A*) 5 min, (*C*) 10 min, (*D*) 20 min, (*E*) 30 min, (*F*) 1 h, and (*G*) 8 h in methanol at a concentration of 0.5 mg/mL, (*B* and *H*) the corresponding enlarged AFM images of dashed boxes in *A* and *G*, and (*I*) a plot of L_n as a function of heating time (also summarized in *SI Appendix*, Table S3).

aggregation numbers of the micelles (41). Further, plots of L_n as a function of temperature show that L_n increases dramatically with increasing temperature in all cases (*SI Appendix*, Fig. S8*C*). This may be associated with the increased compatibility of the PNOG in methanol upon heating, which facilitates the rearranging of the chains into longer fibers.

We further added fresh polymer to a sample of annealed spines. Bulk PEG_{112}-*b*-$PNOG_{54}$ (1 mg) was added to a solution (0.5 mg/mL) after 2-h incubation at 60 °C. The L_n of the fibers was observed to grow substantially, reaching up to 910 nm, an increase of ∼240 nm as compared to the original solution without addition. This indicates that the spines can template their own further elongation upon the addition of more polymers (*SI Appendix*, Fig. S10 *A* and *B*). Freshly added polymer quickly forms spherical micelles in hot methanol, which subsequently fuse with one another into a necklace-like morphology. Fiber growth directly from soluble unimers is unlikely to occur, considering the poor solubility of the polypeptoid in methanol (Scheme 1). A second addition of 1 mg PEG_{112}-*b*-$PNOG_{54}$ bulk sample to the previous solution resulted in a further rise of the L_n by ∼150 nm (*SI Appendix*, Fig. S10*C*). This suggests that the added samples partially initiate the growth of new fibers as well as add to existing fibers, which deviates from a living growth mechanism. This also indicates that further addition of polymer shifts the equilibrium between spheres and fibers, and enables the fiber growth. Qualitatively similar behavior is seen in other samples with different DP of PNOG (*SI Appendix*, Fig. S11), confirming the conclusion.

Growth of Lateral Fibers Below T_{m1}. The real-time morphology evolution upon cooling of the assembly solution was next studied under various conditions (Fig. 3 *A*–*F*). In the case of PEG_{112}-*b*-$PNOG_{54}$, as described above, AFM revealed the coexistence of the fibers and spheres at 65 °C. No significant morphological differences were observed until the temperature was cooled to 50 °C, in the vicinity of T_{m1}. At this temperature, a few spheres are observed to protrude on the side surface of the core fiber (spine) that enables the growth of lateral fibers. The spheres partially fuse to produce short fibers, which also serve as the growth motifs to provide material into the superbrushes. We plotted the mean contour length of lateral width ($L_{n\text{-lateral}}$) as a function of temperature. The $L_{n\text{-lateral}}$ value increases to ∼67 nm with decreasing the temperature from 50 °C (0.3 °C/min) to room temperature (*SI Appendix*, Fig. S12). Further incubation of the solution at room temperature resulted in the continued growth of the width (Fig. 3 *G*–*L*). It is clearly shown that the lateral assembly is composed of short fibers at room temperature. The $L_{n\text{-lateral}}$ significantly increased up to ∼1.0 μm with a narrow PDI of 1.01 to ∼1.02 in the first 7 h and then reached a plateau. These brush-like superstructures exhibit consistent dimensions across length, width, and height, and are observed to persist after incubation times up to 1 y (*SI Appendix*, Fig. S13), suggesting excellent stability at room temperature. Simultaneously, the number of spheres dramatically decreased and eventually disappeared, which confirms that the brush-like superstructures grow upon the consumption of spherical micelles by coalescence. This also suggests the reorganization of the chains during the brush formation process. Both AFM and TEM imaging confirm this intermediate morphology and fusion process (*SI Appendix*, Fig. S14). Additionally, the necklace-like morphology of the core fiber is distinctly seen, which confirms the sphere-to-fiber fusion mechanism. It further explains the exclusive formation of lateral fibers instead of extended nanosheet-like structures. The necklace morphology contains a regular latitudinal pattern, with varying chain packing patterns and densities of PEG on the surface, which results in the periodic initiation of lateral fiber growth. It is likely that one of these domains contains more well-ordered and solvent-exposed PNOG chains, which behave as the seed to initiate further growth of the lateral fibers. In order to verify this assumption, we repeated the entire assembly process in 2% chloroform in methanol (vol/vol). Chloroform is known to well dissolve both blocks. As the temperature decreased from 65 °C to room temperature, only spheres were observed, due to the enhanced solubility of the solvent for both blocks (*SI Appendix*, Fig. S15). Further incubation of the solution at room temperature resulted in the formation of two-dimensional (2D) nanosheet structures, instead of brushes (Scheme 1). Thus, the preassembled necklace-like structure is very critical for the propagation of superbrushes. The diameter of the lateral fibers of brushes is ∼21.2 nm, nearly identical to the diameter of spherical micelles, while the height of the lateral fibers is ∼6.2 nm, ∼5 nm to 6 nm lower than that of the spines. This is possibly due to the distinct molecular packing geometry, which suggests the

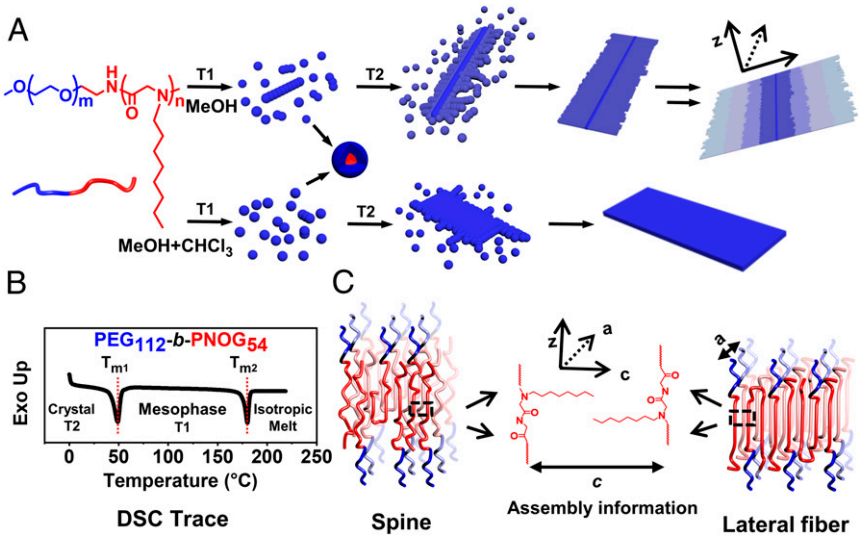

Scheme 1. (*A*) Brush-like superstructures and nanosheets of the crystalline diblock copolymers. The characteristics of the brush-like superstructures represent the samples PEG_{112}-*b*-$PNOG_{54}$. T1 and T2 represent mesophase and crystal regions, respectively. (*B*) Typical DSC trace of diblock copolymer. (*C*) Detailed structure of both spine and lateral fiber.

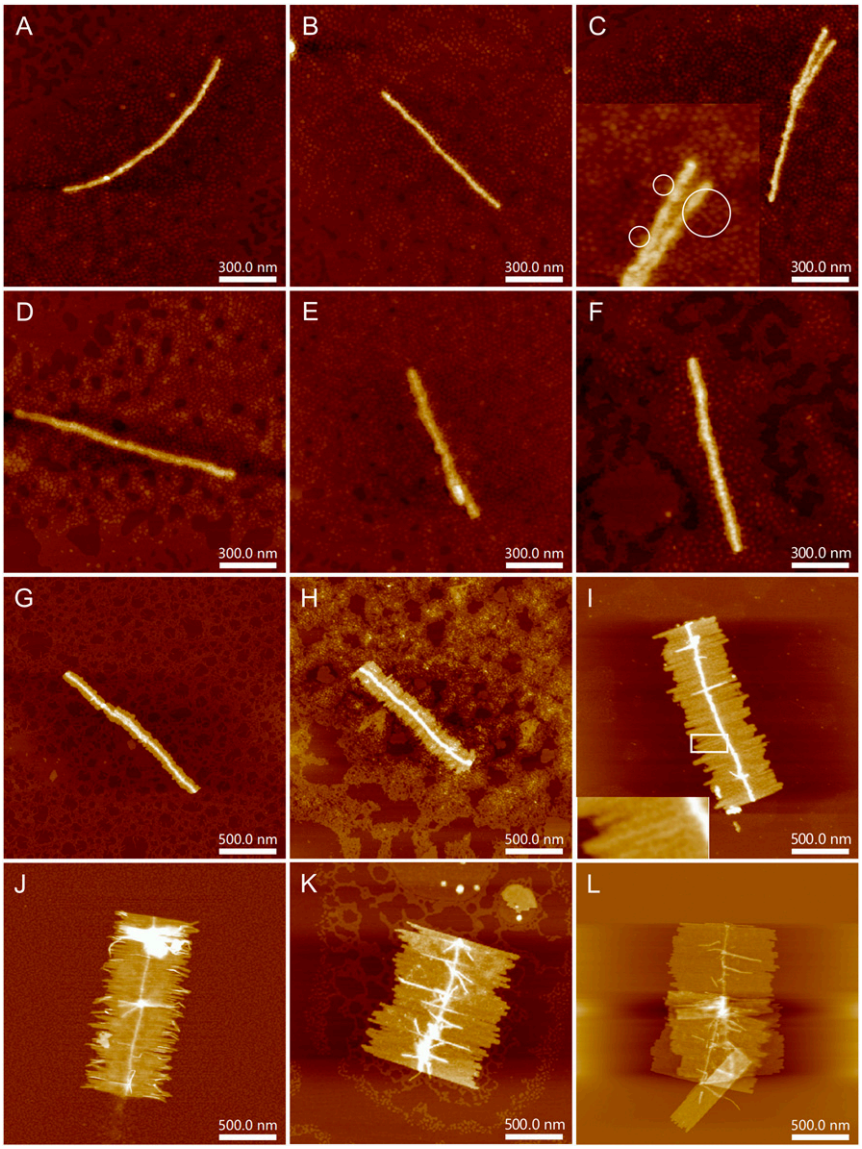

Fig. 3. Real-time morphology evolution upon cooling. AFM images of PEG_{112}-*b*-$PNOG_{54}$ cooled to various temperatures of (*A*) 65 °C, (*B*) 60 °C, (*C*) 50 °C, (*D*) 40 °C, (*E*) 30 °C, and (*F*) 25 °C at a rate of 0.3 °C/min and incubated for (*G*) 1 h, (*H*) 1.5 h, (*I*) 3 h, (*J*) 4 h, (*K*) 7 h, and (*L*) 24 h after annealing at 65 °C for 2 h in methanol at a concentration of 0.5 mg/mL. Circled regions in *C* indicates initial sites of lateral fiber growth. Insets in *C* and *I* indicate magnified regions.

cooling process is accompanied by the rearrangement of PNOG and PEG chains. Note that the thickness of the nanosheets formed in 2% chloroform (~6.3 nm) is consistent with the height of the lateral fibers. Thus, PNOG likely exhibits similar chain packing in both cases. We have previously prepared well-ordered 2D nanosheets with folded crystalline PNOG chains, which also showed a nearly identical thickness (41). This may suggest that, in the current study, the PNOG in both lateral fiber and the nanosheet adopts a thermodynamically favored, folded chain packing. The fusion of lateral-arrayed fibers into a flat sheet-like region is occasionally observed, as indicated by microscopy images. We, indeed, have previously shown that the lateral-arrayed fibers from phenyl-containing polypeptoid copolymers tend to fuse into nanosheets (42). It is also noted that the central spine length, L_n, remains quite consistent during the entire cooling process (*SI Appendix*, Fig. S16), suggesting that lateral growth is preferred upon cooling. This is possibly due to the degree of organization in the solvent-exposed faces of the PNOG domain, similar to the periodicity on the side surface of the spine as mentioned above.

Molecular Packing within the PNOG Domain. Insight into the detailed molecular packing of the nanobrush assemblies was provided by grazing incidence wide-angle X-ray scattering (GIWAXS). We prepared dry samples by evaporating the corresponding solvents at the same preparation temperature. The in-plane line profiles of the assemblies at different time intervals are shown in *SI Appendix*, Fig. S17. Generally, the scattering patterns are associated with Bragg reflections of PNOG crystals. We used GIWAXS to probe the structural evolution of the PNOG domain as a function of temperature. At 65 °C, the scattering peak at $q = q^* = 3.0$ nm^{-1}, denoted as the (001) plane, is taken to correspond to the characteristic distance between adjacent backbones, *c*, by $d = 2\pi/q^* = 2.1$ nm. Higher-order peaks at $2q^*$ and $3q^*$ indicate the presence of a lamellar structure. This characteristic peak represents the typical packing mode of crystalline polypeptoids that we use here to direct the assembly (41). One broad peak corresponding to the (100) reflection gives the interchain distance, *a,* of 4.6 Å. The broad peaks observed suggest less ordered interchain packing. As the system is cooled to room temperature, one additional peak is observed, as the

reflection from the (103) plane at 3.8 Å. After 24 h at room temperature, the intensity of this peak increases, and a prominent peak in the vicinity of q = 15.7 nm^{-1} also becomes visible, related to reflections from the (102) plane. The reflections of (102) and (103) correspond to the long-range correlation between the c and a directions (43). This indicates that the crystallinity of the PNOG domain increases with incubation time at room temperature, confirming the rearrangement of the PNOG chains during the assembly process. These results coincide well with the DSC results of bulk samples, and the sanidic liquid crystalline-phase behavior previously reported for *N*-alkyl polypeptoid copolymers (43). Specifically, as the temperature increases to T_{m1}, a sanidic mesophase is achieved, possessing conformational disorder restricted in dimensions normal to c direction. Note that PEG is highly solvated in methanol, indicated by the absence of its typical crystalline peak. The fully stretched end-to-end length of $PNOG_{54}$ is calculated to be ~20.1 nm by GIWAXS (41), much larger than the heights of both spines and lateral fibers. Thus, it is likely that the PNOG core contains some combinations of folded crystalline chains and disordered regions in the superbrush. The distinct geometry of the spine, in contrast to the lateral fiber, is likely a result of the different degree of crystallinity in each domain. The spine, formed at elevated temperature, possesses more mobile chains with larger aggregation numbers. The lateral fibers contain an increased fraction of crystalline PNOG folds that result in smaller height, consistent with the nanosheets from the same block copolymer in ethanol previously reported (41). This suggests a similar crystalline packing geometry. The crystalline properties of the superstructure were further confirmed by DSC, which exhibits apparent broadened melting peaks at ~50 °C and 180 °C with shoulders (*SI Appendix*, Fig. S18).

Proposed Nanobrush Self-Assembly Mechanism. Based on these data, we propose the formation mechanism for crystalline brush-like superstructure in Scheme 1. The sphere-like micellar subunits are initially formed and then begin to connect primarily via solvophobic interactions into roughly linear assemblies, or spines, with a necklace-like architecture. This micellar fusion is likely the result of chain mobility within the PNOG domain in the mesophase at elevated temperature (> T_{m1}), which is in a good agreement with the classical theory of crew-cut micelles (38). In those systems, the formation of micelles is controlled by a force balance involving three factors, including the stretching of the core-forming blocks in the core, the surface tension, and the intercorona chain interactions. It is likely that the PNOG chains stretch upon micellar fusion to facilitate the increased aggregation number, as indicated by the increased height of the spine. Note that the X-ray scattering peak at q = 2.1 nm, denoting the c distance between adjacent backbones, persists during this process. Unlike the entirely amorphous core of a coil–coil copolymer, the chain packing within PEG-*b*-PNOG assemblies is partially ordered, which serves to direct the entire assembly. It is conceivable that the micelles fuse through the c direction packing on the *ac* plane of the PNOG domains to further organize and stretch into anisotropic spine structures. Upon cooling, this packing asymmetry acts as stored assembly information to template the further planar lateral growth from the spine in opposed direction. In addition, due to the presence of the ordered domains within the spine, its morphology becomes locked upon cooling. The necklace-like seeds offer periodic nucleation sites arising from their origin as fused spheres. This may result in two regions with different surface tensions (44). The regular fluctuation of PEG density arising from necklace morphology may result in periodic display of ordered PNOG domains on the spine. These ultimately result in the lateral growth of discrete fibers instead of flat 2D nanosheets. In contrast to the assembly being mainly driven by solvophobic interactions at elevated temperature, the free energy of PNOG crystallization dominates the aggregation behavior of the system at lower temperature. The degree of crystallinity of the PNOG core is controllable with temperature, which determines the packing pattern of the core blocks and optimizes the balance between the interfacial energy and the crystallization energy. All these factors facilitate the hierarchical formation mechanism of the nanobrush superstructures from a single type of block copolymer in a one-pot preparation.

We further investigated the mean contour length of the lateral fibers ($L_{n\text{-lateral}}$) systematically (*SI Appendix*, Figs. S19–S21 and Table S5). Similar to the L_n dependence on DP, the $L_{n\text{-lateral}}$ values decrease with increasing the DP of PNOG. This is possibly due to the less mobile PNOG chains with higher DP. Conversely, both increasing temperature and reducing the cooling rate can largely facilitate the long-range ordered packing, which enables increased $L_{n\text{-lateral}}$. Note that the brush-like superstructures are rarely formed as the solution is heated to 50 °C or below, which is just below the first melting transition. This confirms that the phase transition into a mesophase is a prerequisite for the formation of the assemblies. Further, increasing the polypeptoid concentration induces an obvious decrease in $L_{n\text{-lateral}}$. We have demonstrated that L_n of the core fiber increases with increasing the concentration, which results in a large number of the core fibers and a small molar ratio of growth units to seeds. Thus, the resultant superbrush shows elongated morphology with short lateral brush lengths. Decreasing the concentration to lower than 0.25 mg/mL results in the absence of the assemblies, indicating the critical role of concentration (*SI*

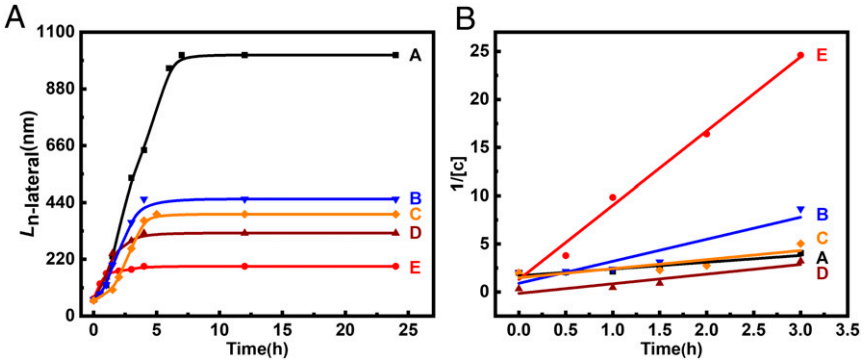

Fig. 4. L_n and (1/[c]) as function of incubation time. (*A*) A plot of L_n versus time. (*B*) A plot of polymer (1/[c]) versus time. Line A represents PEG_{112}-*b*-$PNOG_{54}$ cooled at a rate of 0.3 °C/min after annealing at 65 °C for 2 h in methanol at a concentration of 0.5 mg/mL. Line B represents PEG_{112}-*b*-$PNOG_{74}$ cooled at a rate of 0.3 °C/min after annealing at 65 °C for 2 h in methanol at a concentration of 0.5 mg/mL. Line C represents PEG_{112}-*b*-$PNOG_{54}$ cooled at a rate of 0.3 °C/min after annealing at 65 °C for 2 h in methanol at a concentration of 3 mg/mL. Line D represents PEG_{112}-*b*-$PNOG_{54}$ cooled at a rate of 0.3 °C/min after annealing at 60 °C for 2 h in methanol at a concentration of 0.5 mg/mL. Line E represents PEG_{112}-*b*-$PNOG_{54}$ cooled at a rate of 1 °C/min after annealing at 65 °C for 2 h in methanol at a concentration of 0.5 mg/mL. The characteristics are summarized in *SI Appendix*, Tables S6–S10.

Appendix, Fig. S22). In the case of PEG_{112}-*b*-$PNOG_{74}$ with the highest DP of PNOG, the assemblies show trivial dependence on these external factors. We attribute this to the low chain mobility of PNOG in the solvent. The influence of the *n*-alkyl branches structure on the self-assemblies was further investigated (*SI Appendix*, Figs. S23 and S24). Interestingly, the block copolymer poly(ethylene glycol)-*block*-poly(*N*-hexylamine) (PEG-*b*-PNHG) with shorter alkyl side chains forms spherical nanoparticles exclusively, with diameters in a range of 65 nm to 150 nm. We attribute this to the increased solvophilic property of the PNHG block with decreased alkyl chain length. The swollen PNHG chains reduce the interfacial energy of the micelles and can barely crystallize in solution. Both factors inhibit the fusion of the micelles, while the block copolymer poly(ethylene glycol)-*block*-poly(*N*-dodecylamine) (PEG-*b*-PNDG), with longer alkyl side chains, forms irregular aggregates, possibly due to the increased solvophobic property of PNDG. These results suggest that the octyl side chain structure is critical to modulate the solvophilic/solvophobic balance to form the subunits for hierarchical fabrication.

To explore the growth kinetics of self-assembly, we plotted the $L_{\text{n-lateral}}$ as a function of incubation time at room temperature. In each case, the $L_{\text{n-lateral}}$ initially increases with time and eventually levels off (Fig. 4*A*). The absence of growth units including spheres and short fibers suggests the complete conversion of polymers. Note that the block copolymer single chain is barely present in solution, as the PNOG block is incompatible with methanol over the entire experimental range. A plot of conversion rate (α) versus incubation time is addressed in *SI Appendix*, Fig. S25*A*. Despite various DP of the PNOG, the concentration, the temperature, and cooling rate, all of the data share a similar trend, indicative of similar growth kinetics. This is further confirmed by a nearly identical growth rate constant from a linear fitting (*SI Appendix*, Fig. S25*D* and Tables S6–S10). The linear relationship is shown in the plots of the reciprocal of concentration of free polymer versus time (1/[c]) (Fig. 4*B*), which suggests a second-order nature.

For a deep understanding of the mechanism, we explored the growth of heteronanobrushes by using distinct analogs during each step growth. *SI Appendix*, Fig. S26 displays AFM images of an initial superbrush solution of PEG_{112}-*b*-$PNOG_{61}$, with a lateral length of 210 nm and a PDI of 1.02. As 0.125 mg of PEG_{112}-*b*-$PNOG_{61}$ in chloroform was added at room temperature, the lateral length increased to ∼331 nm with the same PDI. Note that the final chloroform concentration is maintained below 5% (vol/vol) to prevent dissociation of the assemblies. Further continued addition of PEG_{112}-*b*-$PNOG_{61}$ resulted in continued lateral growth with a narrow and consistent PDI. A linear plot of $L_{\text{n-lateral}}$ versus the amount of added polymer suggests the absence of self-seeding in the growth process (Fig. 5*A*). We further plotted $L_{\text{n-lateral}}$ as a function of m_{growth}/m_{seed}, where m_{growth} and m_{seed} represent the mass of added polymer and initial polymer, respectively (Fig. 5*B*). The similar linear dependence confirms the living self-assembly manner, which resembles the typical living crystallization-driven self-assembly system (7, 23, 24, 28–30). We performed the experiments by adding different amounts of polymers for three separately repeated experiments. Remarkably, all of the data collapse onto the single line, suggesting excellent reproducibility.

The detailed growth process is further revealed by AFM images, shown in *SI Appendix*, Fig. S27. The spheres protruding on the spine are observed in the process of providing material for the growth of lateral fibers, which is very similar to the assembly of brushes without intermediate addition of polymers, as discussed. The termini of lateral brushes, with their PNOG core, remain active for further growth. This is distinctly different from all reported crystallization-driven living self-assembly, where single polymer chains (also referred as unimers) are considered as the adding species. In our case, less ordered spherical micelles are obtained initially, which is kinetically favored, rather than the hierarchical structure with considerable long-range ordering. As a matter of fact, a related hierarchical assembly pathway is known to occur for the crystallization of some proteins and other molecules in nature, referred to as a crystallization by particle attachment mechanism (32). Instead of direct monomer-by-monomer addition, these crystals grow from amorphous or less crystalline clusters via multiple steps (1). Such a pathway allows the chain to rearrange its interactions for the thermodynamically favorable transition from the initial micelles to hierarchical assemblies. Note that a small amount of polymer unimers may also exist for the growth of the superstructure, which are indiscernible by AFM. Further, a short region of slightly increased height of the lateral fibers is observed after further addition of polymer, which is possibly due to some disordered packing on the growth termini (*SI Appendix*, Fig. S26*G*). To confirm this, we added 0.5 mg of sample into solution right after the solution was cooled to room temperature. For comparison, the same amount of sample was added after complete consumption of growing motifs. It is clearly seen that both $L_{\text{n-lateral}}$s are comparable, while the growth boundary is merely visible from the latter one (*SI Appendix*, Fig. S28). This confirms that the height variation arises from the less ordered geometry present at the growth termini. Note that the $L_{\text{n-lateral}}$ after a heating–cooling cycle differs from the original one. This is because the addition of polymers causes an increase in the concentration that determines the L_n at elevated temperature. Similarly, the addition of block copolymers with different DPs can also induce the length increase of the lateral fibers in a living manner (*SI Appendix*, Fig. S29). Note that the heights are slightly different from one other, which can be associated with the different DP of PNOG.

Thermoreversible Behavior of the Brushes. Remarkably, the brush-like superstructures exhibit thermoreversible behavior. The lateral brushes are observed to disappear or redisperse into the solution and leave the core fiber intact in solution at elevated temperature (*SI Appendix*, Fig. S30). A previous report shows that a diblock copolymer with a crystalline polyferrocenyl dimethylsilane domain self-assembled into fibers at room temperature and spheres at elevated temperature due to the disappearance of the crystallinity (21). In our case, an increase in temperature facilitates the PNOG transition into a mesophase. The increased chain mobility results in the disassembly of the lateral fibers. By contrast, the spine that was formed at elevated temperature has higher stability with embedded *c* distance as assembly information. Thus, it can again be used as a template for further growth upon cooling. As expected, the nanobrushes are reformed, with the exact original dimensions upon cooling. We thus designed a set of four different assembly conditions (1–4) by varying three parameters including temperature, cooling rate, and concentration of polymers (Fig. 5*C* and *SI Appendix*, Fig. S31). Interestingly, the final morphology and dimensions of the brushes obtained were independent of the assembly pathways, and thus the process is completely reversible between these conditions. This offers a nice circle in Fig. 5*C*, indicating assembly is irrelevant to kinetics. We therefore demonstrate that the assembly is a thermodynamic controlled process, confirming the proposed mechanism. Similarly, we observed that the L_n also exhibits a nice reversible circle by varying the temperature and the concentration of polymer (Fig. 5*D*), irrespective of the pathways.

Conclusion

In conclusion, by delicately tuning segmental crystallinity as encoded assembly information and optimizing the crystallization–solvophobicity balance, we prepared unprecedented supramolecular planar nanobrush-like structure composed of two distinct packing patterns in a one-pot preparation. We demonstrate that the lateral growth of the hierarchical brush occurs in a living manner, with the preformed brush serving as a template, and the micelles serving as growing units. By a systematic study, we further demonstrate that the self-assembly behavior of PEG-*b*-PNOG copolymers is considerably dependent on the effects of the molecular weight, side chain property, polymer

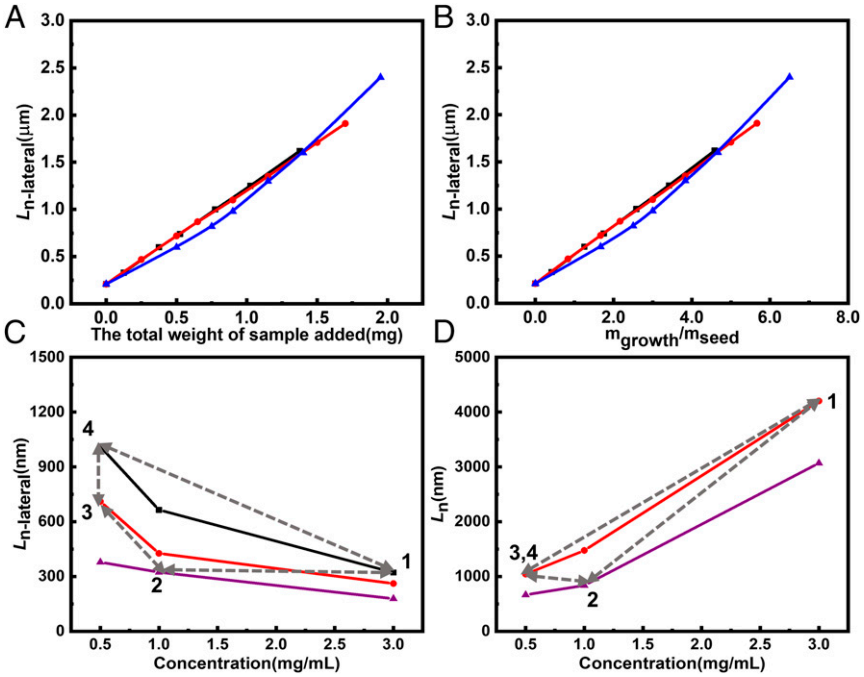

Fig. 5. The brushes exhibiting both living crystallization-driven self-assembly behavior and thermoreversible behavior. (*A* and *B*) Plots of $L_{n\text{-lateral}}$ versus (*A*) the total weight of samples added and (*B*) m_{growth}/m_{seed}. (*C* and *D*) Plots of (*C*) $L_{n\text{-lateral}}$ versus concentration and (*D*) L_n versus concentration. The cycling, as indicated by a gray dashed line, represents the PEG_{112}-*b*-$PNOG_{54}$ reversible assembly processes. The black line represents the PEG_{112}-*b*-$PNOG_{54}$ cooled to room temperature at a rate of 0.3 °C/min and incubated for 24 h after annealing at 65 °C for 2 h in methanol. The red line represents the PEG_{112}-*b*-$PNOG_{54}$ cooled to room temperature at a rate of 0.5 °C/min and incubated for 24 h after annealing at 65 °C for 2 h in methanol. The purple line represents the PEG_{112}-*b*-$PNOG_{54}$ cooled to room temperature at a rate of 0.5 °C/min and incubated for 24 h after annealing at 60 °C for 2 h in methanol. In *A* and *B*, three colors represent three repeated experiments. In *C* and *D*, 1, 2, 3, and 4 represent the four superstructures shown in *SI Appendix*, Fig. S29.

concentration, cooling rate, and temperature. Interestingly, the final morphology and dimension of the brushes are independent of the assembly pathways and are completely thermally reversible. By tuning the subtle interplay of solubility and crystallinity, we show the ability to control the aggregation state and the chain conformation. The ability of a polymer to change its conformation between nearly isoenergetic states is a hallmark of biological systems. Thus, this system has intriguing similarities to polypeptide systems found in misfolded protein diseases (e.g., Alzheimer's disease, Creutzfeldt–Jakob disease, and Parkinson's disease), where a soluble form of a protein undergoes a change of conformation into a more stable, aggregated beta structure.

It is likely that this programmable self-assembly strategy can be extended to other systems by the similar encoding of structural information. In addition, these structures are amenable to surface functionalization, where terminal functional groups/domains can be appended to the PEG domain, and therefore end up being surface displayed. These dry brushes can be simply dispersed into water after drying from methanol (*SI Appendix*, Fig. S32), which can enable biological functions. The excellent biocompatibility combined with the high structural tunability of polypeptoids offers great potential to design precision biomimetic nanostructures for applications in biomedicine and nanotechnology. Many of these investigations are in progress in our laboratory.

Materials and Methods

N-octyl *N*-carboxyanhydride was synthesized according to reported method (36). Tetrahydrofuran (THF) and hexane were first purified by purging with dry N_2, followed by passing through a column of activated alumina. Dichloromethane was stored over calcium hydride (CaH_2) and purified by vacuum distillation with CaH_2. α-Methoxy-ω-amino poly(ethylene glycol) (PEG-NH_2, number-average molecular weight (Mn) = 5000 g/mol, PDI = 1.07) was purchased from JenKem Technology Co, Ltd. All other chemicals were purchased from commercial suppliers and used without further purification unless otherwise noted.

Characterization. The ^{1}H NMR spectra were recorded using Bruker Avance NEO 400-MHz instruments at ambient temperatures. Chemical shifts (δ) were determined using tetramethylsilane as internal reference. Tandem Gel permeation chromatography (GPC) was performed using a pump (Scientific Systems, Inc.) connected to a Wyatt Optilab DSP at a flow rate of 1 mL/min and chloroform (high performance liquid chromatography grade) as an elution solvent. All GPC sample concentrations were 6 mg/mL. Conventional calibrations were performed using polystyrene standards. DSC studies were conducted using a TA DSC 2920 calorimeter with a nitrogen purge rate of 50 mL/min. The 2- to 10-mg sample is placed in an aluminum T-Zero series pan, and the standard lid is compressed. Powder samples sealed into the aluminum pans were first heated from 0 °C to 200 °C at 10 °C/min for three cycles. The assembly sample (0.5 mg/mL) was dried, collected, and stored under ambient conditions before testing. AFM studies were conducted using tapping mode AFM (Bruker Multimode 8 AFM/SPM system) in ambient air with Nanoscope software. Five microliters of polymer solution was placed on the mica by spin-coater, and dried on freshly cleaved mica under ambient conditions before AFM imaging. Minimal processing of the images was done using Nanoscope Analysis software from Bruker. TEM experiments were conducted on an FEI TECNAI 20, with a Gatan digital camera and Gatan Digital Micrograph analysis software. Six microliters of polymer solution was pipetted onto carbon-coated copper grids. The excess solution was removed, and the sample was negatively stained with 1 wt % uranyl acetate. The solvent was evaporated for at least 12 h, except when otherwise noted. Cryo-EM experiments were conducted on the same instrument. The vitrified specimens were prepared using a Vitrobot (FEI, Inc.). A 5-μL droplet of the ethanol solution at a concentration of 1 mg/mL was deposited on the surface of glow-discharged grids with lacey carbon films. The droplet was blotted by filter paper for 2 s, followed by 2 s of draining, and then plunged into liquid ethane to obtain a vitrified thin film. The grids were then transferred to a Gatan cryo-stage at −185 °C for analysis. The GIWAXS measurements were performed with the energy of 10 keV in top-off mode at beamline 7.3.3, Advanced Light Source (ALS), Lawrence Berkeley National Laboratory. The scattering intensity was recorded on a 2D Pilatus 1M detector (Dectris) with a pixel size of 172 μm. A silver behenate sample was used as a standard to calibrate the beam position and the sample–detector distance. The sample (0.5 mg/mL) was deposited on Si wafers, dried, and stored under ambient conditions before testing. For the statistical analysis, a minimum of ∼100

assemblies were carefully traced manually to determine their contour characteristics. The average length of the spine and lateral fiber (L_n, $L_{n\text{-lateral}}$) and weight average micelle length of the spine and lateral fiber (L_w, $L_{w\text{-lateral}}$) were calculated using Eqs. **1** and **2** from measurements of the contour lengths (L_i) of individual assembly, where N_i is the number of assemblies of L_i, and n is the number of assemblies in each sample. The distribution of assemblies lengths is characterized by both L_w/L_n, $L_{w\text{-lateral}}/L_{n\text{-lateral}}$ and the SD of the length distribution σ.

$$L_n, L_{n-lateral} = \frac{\sum_{i=1}^{n} N_i L_i}{\sum_{i=1}^{n} N_i} \quad [1]$$

$$L_w, L_{w-lateral} = \frac{\sum_{i=1}^{n} N_i L_i^2}{\sum_{i=1}^{n} N_i L_i}. \quad [2]$$

Synthesis of PEG-*b*-PNOG Diblock Copolymers. The synthetic procedure of diblock copolypeptoids containing a hydrophobic *N*-alkylglycine peptoid block and a polar PEG block by ROP of NNCA monomers with mPEG-NH_2 (Mn = 5,000) as the initiator (*SI Appendix*, Fig. S1) (36). In a typical procedure, mPEG-NH_2 (102.3 mg, Mn = 5,000 g/mol) was heated and melted at 85 °C, dried under high vacuum for 24 h, and then dissolved in anhydrous THF to obtain a 15% PEG solution. In a glove box, 261 mg of n-octyl-*N*-carboxy anhydride monomer was dissolved in anhydrous THF (3 mL) and then added to the reaction flask with the given ratio. The polymerization was carried out at 55 °C for 24 h under a N_2 atmosphere, and then the solution was precipitated in an excess of diethyl ether. The white precipitate was collected and washed with sufficient methanol and diethyl ether. The product was dried under vacuum to give a white solid (165 mg, 53% yield). All of the other samples including poly(ethylene glycol)-*block*-poly(*N*-dodecylamine) and poly(ethylene glycol)-*block*-poly(*N*-hexylamine) were prepared in a similar manner, depending on the designated ratio of monomer to initiator.

Self-Assembly of PEG-*b*-PNOG Diblock Copolymers. The polymer was first dispersed in methanol in a clean vial and heated to the desired temperature for different time intervals. The solution was slowly cooled to room temperature at different rates and aged at room temperature. Small aliquots (~5 μL) were obtained from the solution at different time intervals to study the assembly structures. The temperature of the baths was controlled using IKA magnetic stirrer (RCT basic model).

Data Availability. All study data are included in the article and *SI Appendix*.

ACKNOWLEDGMENTS. This work was supported by grants from National Natural Science Foundation of China (51722302 and 21674054), and the Natural Science Foundation of Shandong Province (ZR2019JQ17). The Beamline 7.3.3 at the ALS, the Molecular Foundry, and the Soft Matter Electron Microscopy Program (KC11BN) are supported by the Office of Science, Office of Basic Energy Sciences, of the US Department of Energy under Contract DE-AC02-05CH11231.

1. S. Chung, S.-H. Shin, C. R. Bertozzi, J. J. De Yoreo, Self-catalyzed growth of S layers via an amorphous-to-crystalline transition limited by folding kinetics. *Proc. Natl. Acad. Sci. U.S.A.* **107**, 16536–16541 (2010).
2. P. Fratzl, R. Weinkamer, Nature's hierarchical materials. *Prog. Mater. Sci.* **52**, 1263–1334 (2007).
3. J. W. Bryson *et al.*, Protein design: A hierarchic approach. *Science* **270**, 935–941 (1995).
4. H. K. Murnen, A. M. Rosales, J. N. Jaworski, R. A. Segalman, R. N. Zuckermann, Hierarchical self-assembly of a biomimetic diblock copolypeptoid into homochiral superhelices. *J. Am. Chem. Soc.* **132**, 16112–16119 (2010).
5. K. Miszta *et al.*, Hierarchical self-assembly of suspended branched colloidal nanocrystals into superlattice structures. *Nat. Mater.* **10**, 872–876 (2011).
6. C. Yuan *et al.*, Hierarchically oriented organization in supramolecular peptide crystals. *Nat. Rev. Chem.* **3**, 567–588 (2019).
7. H. Qiu, G. Cambridge, M. A. Winnik, I. Manners, Multi-armed micelles and block co-micelles via crystallization-driven self-assembly with homopolymer nanocrystals as initiators. *J. Am. Chem. Soc.* **135**, 12180–12183 (2013).
8. B. Ni *et al.*, Pathway toward large two-dimensional hexagonally patterned colloidal nanosheets in solution. *J. Am. Chem. Soc.* **137**, 1392–1395 (2015).
9. A. H. Gröschel *et al.*, Precise hierarchical self-assembly of multicompartment micelles. *Nat. Commun.* **3**, 710 (2012).
10. M. Huang *et al.*, Self-assembly. Selective assemblies of giant tetrahedra via precisely controlled positional interactions. *Science* **348**, 424–428 (2015).
11. E. V. Shevchenko, D. V. Talapin, N. A. Kotov, S. O'Brien, C. B. Murray, Structural diversity in binary nanoparticle superlattices. *Nature* **439**, 55–59 (2006).
12. L. Cademartiri, K. J. Bishop, Programmable self-assembly. *Nat. Mater.* **14**, 2–9 (2015).
13. R. N. Zuckermann, Peptoid origins. *Biopolymers* **96**, 545–555 (2011).
14. K. Kirshenbaum, R. N. Zuckermann, K. A. Dill, Designing polymers that mimic biomolecules. *Curr. Opin. Struct. Biol.* **9**, 530–535 (1999).
15. R. N. Zuckermann, T. Kodadek, Peptoids as potential therapeutics. *Curr. Opin. Mol. Ther.* **11**, 299–307 (2009).
16. C. U. Lee, T. P. Smart, L. Guo, T. H. Epps 3rd, D. Zhang, Synthesis and characterization of amphiphilic cyclic diblock copolypeptoids from *N*-heterocyclic carbene-mediated zwitterionic polymerization of *N*-substituted *N*-carboxyanhydride. *Macromolecules* **44**, 9574–9585 (2011).
17. A. M. Rosales, H. K. Murnen, R. N. Zuckermann, R. A. Segalman, Control of crystallization and melting behavior in sequence specific polypeptoids. *Macromolecules* **43**, 5627–5636 (2010).
18. C.-U. Lee, A. Li, K. Ghale, D. Zhang, Crystallization and melting behaviors of cyclic and linear polypeptoids with alkyl side chains. *Macromolecules* **46**, 8213–8223 (2013).
19. C. Secker, A. Völkel, B. Tiersch, J. Koetz, H. Schlaad, Thermo-induced aggregation and crystallization of block copolypeptoids in water. *Macromolecules* **49**, 979–985 (2016).
20. C. Fetsch, J. Gaitzsch, L. Messager, G. Battaglia, R. Luxenhofer, Erratum: Corrigendum: Self-assembly of amphiphilic block copolypeptoids—Micelles, worms and polymersomes. *Sci. Rep.* **6**, 39441 (2016).
21. J. A. Massey *et al.*, Self-assembly of organometallic block copolymers: The role of crystallinity of the core-forming polyferrocene block in the micellar morphologies formed by poly (ferrocenylsilane-*b*-dimethylsiloxane) in *n*-alkane solvents. *J. Am. Chem. Soc.* **122**, 11577–11584 (2000).
22. B. Jin *et al.*, One-pot universal initiation-growth methods from a liquid crystalline block copolymer. *Nat. Commun.* **10**, 2397 (2019).
23. X. Wang *et al.*, Cylindrical block copolymer micelles and co-micelles of controlled length and architecture. *Science* **317**, 644–647 (2007).
24. J. Schmelz, A. E. Schedl, C. Steinlein, I. Manners, H. Schmalz, Length control and block-type architectures in worm-like micelles with polyethylene cores. *J. Am. Chem. Soc.* **134**, 14217–14225 (2012).
25. L. Sun *et al.*, Structural reorganization of cylindrical nanoparticles triggered by polylactide stereocomplexation. *Nat. Commun.* **5**, 5746 (2014).
26. B. Li, C. Y. Li, Immobilizing au nanoparticles with polymer single crystals, patterning and asymmetric functionalization. *J. Am. Chem. Soc.* **129**, 12–13 (2007).
27. J. Xu, Y. Ma, W. Hu, M. Rehahn, G. Reiter, Cloning polymer single crystals through self-seeding. *Nat. Mater.* **8**, 348–353 (2009).
28. D. Tao *et al.*, Monodisperse fiber-like micelles of controlled length and composition with an oligo (p-phenylenevinylene) core via "living" crystallization-driven self-assembly. *J. Am. Chem. Soc.* **139**, 7136–7139 (2017).
29. S. K. Patra *et al.*, Cylindrical micelles of controlled length with a π-conjugated polythiophene core via crystallization-driven self-assembly. *J. Am. Chem. Soc.* **133**, 8842–8845 (2011).
30. J. Qian *et al.*, Self-seeding in one dimension: An approach to control the length of fiberlike polyisoprene-polyferrocenylsilane block copolymer micelles. *Angew. Chem. Int. Ed. Engl.* **50**, 1622–1625 (2011).
31. D. R. Greer *et al.*, Liquid-crystalline phase behavior in polypeptoid diblock copolymers. *Macromolecules* **51**, 9519–9525 (2018).
32. J. J. De Yoreo *et al.*, Crystal growth. Crystallization by particle attachment in synthetic, biogenic, and geologic environments. *Science* **349**, aaa6760 (2015).
33. N. Jiang *et al.*, Crystallization-driven self-assembly of coil–comb-shaped polypeptoid block copolymers: Solution morphology and self-assembly pathways. *Macromolecules* **52**, 8867–8877 (2019).
34. J. R. Edison *et al.*, Conformations of peptoids in nanosheets result from the interplay of backbone energetics and intermolecular interactions. *Proc. Natl. Acad. Sci. U.S.A.* **115**, 5647–5651 (2018).
35. X. Ma *et al.*, Tuning crystallization pathways through sequence engineering of biomimetic polymers. *Nat. Mater.* **16**, 767–774 (2017).
36. Y. Ni *et al.*, Two-dimensional supramolecular assemblies from pH-responsive poly(ethyl glycol)-*b*-poly(l-glutamic acid)-*b*-poly(*N*-octylglycine) triblock copolymer. *Biomacromolecules* **18**, 3367–3374 (2017).
37. E. P. Holowka, D. J. Pochan, T. J. Deming, Charged polypeptide vesicles with controllable diameter. *J. Am. Chem. Soc.* **127**, 12423–12428 (2005).
38. L. Zhang, A. Eisenberg, Thermodynamic vs kinetic aspects in the formation and morphological transitions of crew-cut aggregates produced by self-assembly of polystyrene-*b*-poly (acrylic acid) block copolymers in dilute solution. *Macromolecules* **32**, 2239–2249 (1999).
39. Y. Mai, A. Eisenberg, Self-assembly of block copolymers. *Chem. Soc. Rev.* **41**, 5969–5985 (2012).
40. H. Shen, A. Eisenberg, Morphological phase diagram for a ternary system of block copolymer PS_{310}-*b*-PAA_{52}/dioxane/H_2O. *J. Phys. Chem. B* **103**, 9473–9487 (1999).
41. Z. Shi, Y. Wei, C. Zhu, J. Sun, Z. Li, Crystallization-driven two-dimensional nanosheet from hierarchical self-assembly of polypeptoid-based diblock copolymers. *Macromolecules* **51**, 6344–6351 (2018).
42. Y. Wei *et al.*, Supramolecular nanosheets assembled from poly (ethylene glycol)-*b*-poly (*N*-(2-phenylethyl) glycine) diblock copolymer containing crystallizable hydrophobic polypeptoid: Crystallization driven assembly transition from filaments to nanosheets. *Macromolecules* **52**, 1546–1556 (2019).
43. D. R. Greer *et al.*, Universal relationship between molecular structure and crystal structure in peptoid polymers and prevalence of the *cis* backbone conformation. *J. Am. Chem. Soc.* **140**, 827–833 (2018).
44. T. Vilgis, A. Halperin, Aggregation of coil-crystalline block copolymers: Equilibrium crystallization. *Macromolecules* **24**, 2090–2095 (1991).